Computational Modeling of Laser Welding of Cu-Ni Dissimilar Couple

GANDHAM PHANIKUMAR, PRADIP DUTTA, and KAMANIO CHATTOPADHYAY

A three-dimensional transient model to solve heat transfer, fluid flow, and species conservation during laser welding of dissimilar metals is presented. The model is based on a control volume formulation with an enthalpy-porosity technique to handle phase change and a mixture model to simulate mixing of molten metals. Weld pool development, solidified weld pool shape, and composition profiles are presented for both stationary as well as continuous laser welding in conduction mode. Salient features of a dissimilar Cu-Ni weld are summarized and thermal transport arguments are employed to successfully explain the observations. It is found that the weld pool shape becomes asymmetric even when the heat source is symmetrically applied on the two metals forming the couple. It is also observed that convection plays an important role in the development of weld pool shape and composition profiles. As the weld pool develops, the side melting first (nickel) is found to experience more convection and better mixing. Results from the case studies of computation are compared with corresponding experimental observations, showing good qualitative agreement between the two.

I. INTRODUCTION

FUSION welding is an important manufacturing technique that has attained a state of maturity in the past few decades. The physical processes that take place during fusion welding, namely, heat transfer, melting, Marangoni convection, electromagnetic and buoyancy forces, and solidification, are well documented.[1,2,3] Microstructure of the weldment, which determines the mechanical properties of the product, is understood in terms of grain structure and phase formation as a function of processing parameters.[4] Several computational studies have also successfully shown insights into the physical processes that occur during welding.[5–11] Convection in the weld pool is now recognized as one of the important processes that determine weld pool characteristics such as size and shape.[12–16] Experimental verification of computational models and prediction of weld pool characteristics as a function of processing conditions have also been relatively successful.[17,18]

However, much of the work on numerical simulation of welding is in the context of joining of similar metals and alloys. Recent advances in manufacturing industry require dissimilar metals and alloys to be joined. Studies on the extension of current understanding of welding of similar metals/alloys to that of dissimilar metals/alloys are limited.[19,20] It is found that a majority of the existing literature on the joining of dissimilar metals and alloys is mainly concentrated on steels and the problem should be analyzed in a case-by-case manner. The quality of weld assessed for several metals is used to decide if a combination is weldable.[21] It may be noted, however, that microstructural features that emerge due to differences in the physical properties of the two metals could be very different from the features observed in welding of similar metals/alloys.[22] The asymmetric shape of the weld, mixing patterns, and solidification microstructure are not well understood. In view of the preceding complications, existing computational models of welding cannot be extended to dissimilar welding in a straightforward manner. The main difficulty arises from the sharp variation of physical properties within the weld pool resulting from composition gradients. Hence, from a scientific standpoint also, analysis of a dissimilar metal joint offers a number of challenges.

The literature reveals that computational studies on welding of dissimilar metals are limited.[22–26] To the best of our knowledge, the only attempts on numerical modeling of dissimilar welding, apart from those by the present authors,[22,23] are by Wei and co-workers.[24,26] Wei *et al.*[26] used a volume of fluid approach along with the SIMPLE algorithm[27] to solve nondimensional temperature, velocity, and composition distribution in the melt pool of a dissimilar joint using a two-dimensional transient formulation. A flat free surface with Gaussian heat source and constant average physical properties was considered. Asymmetry in the flow pattern, and thus, the shape of the weld pool, was highlighted.

Dissimilar metals welding, however, is three-dimensional in nature even in a spot welding mode because of the asymmetry created by the difference in properties of the two metals being welded. In the present article, we demonstrate a three-dimensional transient computational model of laser welding of a dissimilar binary couple of copper and nickel. The associated transport phenomenon and its role in the weld pool development are discussed. The welding is assumed to be in conduction mode and no keyhole formation is considered. The primary objective is to obtain a good insight for understanding some of the physical processes that take place in dissimilar welding. The binary system of copper and nickel is suitable for the present study as it has a simple isomorphous phase diagram (Figure 1) without any miscibility gap or intermetallic compound. Also, these two metals have significant difference in thermophysical properties (Table I), so that the main issues are highlighted. Experimental validation in terms of detailed compositional mapping and weld pool shape is also presented.

GANDHAM PHANIKUMAR, Graduate Student, and KAMANIO CHATTOPADHYAY, Professor, Department of Metallurgy, and PRADIP DUTTA, Associate Professor, Department of Mechanical Engineering, are with the Indian Institute of Science, Bangalore 560012, India. Contact e-mail: pradip@mecheng.iisc.ernet.in

Manuscript submitted March 18, 2003.

II. COMPUTATIONAL MODEL

A schematic diagram of the computational domain used for numerical simulation is shown in the Figure 2(a). Two pieces of copper and nickel with equal dimensions are kept in a butt joint arrangement. A laser heat input with a Gaussian distribution is applied on the top at the centerline of the butt joint such that the heat is distributed equally on both pieces. For a continuous welding process, melting and solidification take place simulatenously, as shown in Figure 2(b). However, during spot welding, melting is a distinct stage during the application of the laser, followed by a solidification process after the laser is switched off (assuming there is no remelting). It may be noted that any mixing of metals due to convection occurs only after the material is molten. Melting and mixing processes at a macroscopic level are modeled by considering both stationary and continuous welding situations of a copper-nickel couple. A locally homogeneous mixture model is considered for the present study, where flow is characterized by the properties assigned according to the relative proportion of each phase in the mixture. Although some information regarding the interface related quantities will be lost, the locally homogeneous model study would still give some insight into this complex problem with regard to flow field, asymmetry of pool shape, temperature field, and mixing.

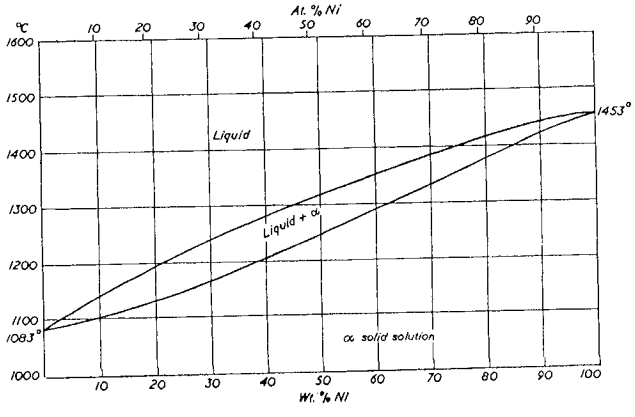

Fig. 1—Phase diagram of copper nickel system.[28]

The following are the assumptions made in the model.

1. The weld pool surface is flat.
2. The fluid motion in the melt pool is assumed to be laminar and incompressible and driven by buoyancy and surface tension gradient (Marangoni) forces.
3. Laser power is distributed in a Gaussian manner at the top surface. The coupling coefficient (laser power efficiency) remains uniform and constant.
4. Thermophysical properties are taken to be different for solid and liquid metals, and variation with temperature is taken into consideration using a smooth fit over the data available in the literature.[28] The expressions used are given in Table I. The physical properties also vary according to the concentration of the mixture, and are evaluated according to mixture theory.
5. Welding is in conduction mode.

The copper-nickel system chosen is very close to an ideal binary system with complete miscibility in liquid and solid states, and hence it justifies most of the assumptions made with regard to the mixture model. One important property that is difficult to estimate for the simulation is the efficiency of heat absorption from the laser beam. While the surface finish and emissivity reduce the coupling efficiency, vapor and plasma formation on the surface of the melt pool enhance the same. It is difficult to determine the coupling efficiency from direct experiments, and published data on this issue are not adequate. An efficiency value close to what is generally found in the literature of laser welding normally near the melting point of the metals (~0.2) is used for the present study. It is found that a variable efficiency leads only to an additional unknown quantity in the model but makes no significant difference to the issues being studied in the present work. Phase change is modeled using an enthalpy-porosity technique.[29] For a given control volume, pure metal properties (including latent heat of fusion) are used until melting takes place. Melting is followed by transport of material from one zone to another and subsequent mixing of the two metals during which the mixture rules for all properties are applied. For continuous welding, additional terms need to be taken into account and are described subsequently in this section.

It is now well recognized that turbulence plays an important role in transport phenomena during welding.[30–37] In this study on dissimilar welds, the scale of mixing of the molten metals is identified to be an important factor during solidification of

Table I. Temperature-Dependent Parameters Used in the Calculations[28]

Property	Expression
k_{Cu} (Wm^{-1}K^{-1})	$393.688 + 0.0096T - 0.0002T^2$ $(T \le T_M)$ $47.56903 + 0.185042T - 8.4054 \times 10^{-5}T^2 + 1.25748 \times 10^{-8}T^3$ $(T_M < T < T_{BOIL})$
k_{Ni} (Wm^{-1}K^{-1})	$90.420288 - 0.1097862T + 1.1856 \times 10^{-4}T^2 - 4.997 \times 10^{-8}T^3 + 7.196 \times 10^{-12}T^4$
c_{Cu} (JKg^{-1}K^{-1})	$376.7528 + 0.143199T - 4.9657144 \times 10^{-5}T^2 + 4.6515071 \times 10^{-9}T^3$
c_{Ni} (JKg^{-1}K^{-1})	$452.725 + 0.2895T - 1.63786 \times 10^{-4}T^2 - 4.997 \times 10^{-8}T^3 + 7.1961 \times 10^{-12}T^4$
μ_{Cu} (Nsm^{-2})	$0.309 \times 10^{-3}\, e^{(30500/8.3147)}$
μ_{Ni} (Nsm^{-2})	$0.1663 \times 10^{-3}\, e^{(50200/8.3147)}$
σ_{Cu} (Nm^{-1})	$1.285 - 0.13 \times 10^{-3}\,(T - T_M)$
σ_{Ni} (Nm^{-1})	$1.778 - 0.38 \times 10^{-3}\,(T - T_M)$
ϕ (any property)	$\phi = \phi_{Cu}C + \phi_{Ni}\,(1 - C)$

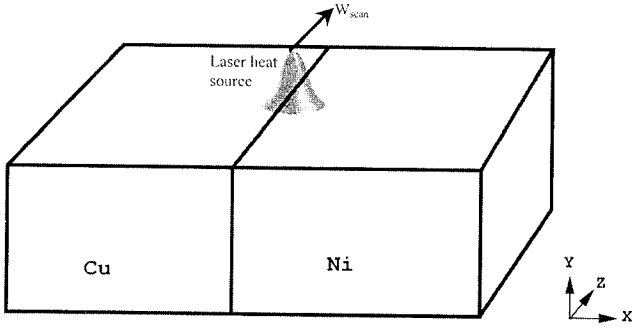

(*a*)

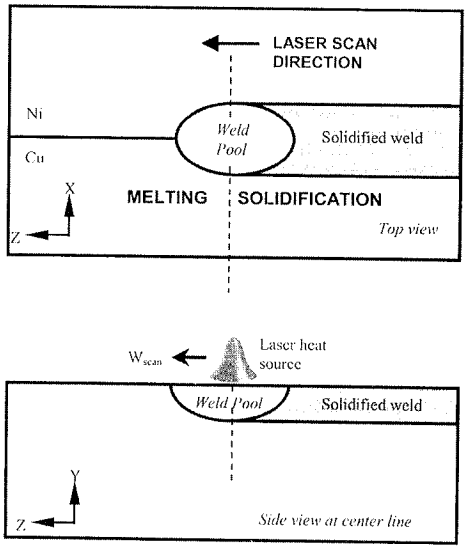

(*b*)

Fig. 2—(*a*) Schematic of laser welding setup. (*b*) Schematic illustrating simultaneous melting and solidification during continuous welding.

the weld, and turbulence can play a significant role in mixing at a local scale. The locally homogeneous mixture model used in the present study may take care of some of the turbulence effects regarding enhanced mixing at a local scale. Also, it may be noted that in this preliminary model, we are focusing on some other important issues of dissimilar metal welding, and the role of turbulence is intended to be studied in the future. The conservation equations for mass, momentum, enthalpy, and species for laminar flow are given subsequently. The source terms (S) are presented in detail for spot and continuous welding in the corresponding subsections.

Continuity:

$$\frac{\partial \rho}{\partial t} + \frac{\partial}{\partial x}(\rho u) + \frac{\partial}{\partial y}(\rho v) + \frac{\partial}{\partial z}(\rho w) = 0 \qquad [1]$$

Momentum:

$$\frac{\partial}{\partial t}(\rho u) + \frac{\partial}{\partial x}(\rho u u) + \frac{\partial}{\partial y}(\rho v u) + \frac{\partial}{\partial z}(\rho w u) = \frac{\partial}{\partial x}\left(\mu \frac{\partial u}{\partial x}\right) + \frac{\partial}{\partial y}\left(\mu \frac{\partial u}{\partial y}\right) + \frac{\partial}{\partial z}\left(\mu \frac{\partial u}{\partial z}\right) - \frac{\partial p}{\partial x} + S_x \qquad [2]$$

$$\frac{\partial}{\partial t}(\rho v) + \frac{\partial}{\partial x}(\rho u v) + \frac{\partial}{\partial y}(\rho v v) + \frac{\partial}{\partial z}(\rho w v) = \frac{\partial}{\partial x}\left(\mu \frac{\partial v}{\partial x}\right) + \frac{\partial}{\partial y}\left(\mu \frac{\partial v}{\partial y}\right) + \frac{\partial}{\partial z}\left(\mu \frac{\partial v}{\partial z}\right) - \frac{\partial p}{\partial y} + S_y \qquad [3]$$

$$\frac{\partial}{\partial t}(\rho w) + \frac{\partial}{\partial x}(\rho u w) + \frac{\partial}{\partial y}(\rho v w) + \frac{\partial}{\partial z}(\rho w w) = \frac{\partial}{\partial x}\left(\mu \frac{\partial w}{\partial x}\right) + \frac{\partial}{\partial y}\left(\mu \frac{\partial w}{\partial y}\right) + \frac{\partial}{\partial z}\left(\mu \frac{\partial w}{\partial z}\right) - \frac{\partial p}{\partial z} + S_z \qquad [4]$$

Energy:

$$\frac{\partial}{\partial t}(\rho H) + \frac{\partial}{\partial x}(\rho u H) + \frac{\partial}{\partial y}(\rho v H) + \frac{\partial}{\partial z}(\rho w H) = \frac{\partial}{\partial x}\left(k \frac{\partial T}{\partial x}\right) + \frac{\partial}{\partial y}\left(k \frac{\partial T}{\partial y}\right) + \frac{\partial}{\partial z}\left(k \frac{\partial T}{\partial z}\right) + S_h \qquad [5]$$

Mass fraction:

$$\frac{\partial C}{\partial t} + \frac{\partial}{\partial x}(u C) + \frac{\partial}{\partial y}(v C) + \frac{\partial}{\partial z}(w C) = \frac{\partial}{\partial x}\left(D \frac{\partial C}{\partial x}\right) + \frac{\partial}{\partial y}\left(D \frac{\partial C}{\partial y}\right) + \frac{\partial}{\partial z}\left(D \frac{\partial C}{\partial z}\right) + S_C \qquad [6]$$

In the preceding equations, t is time; ρ is density; u, v, and w are velocities along x, y, and z directions, respectively; μ is viscosity; p is pressure; k is thermal conductivity; H is enthalpy; C is species concentration; and D is species diffusivity.

A. *Spot Welding*

The source terms in Eqs. [1] through [6] according to the enthalpy-porosity formulation are expressed as follows:

$$S_x = -\left(\frac{K(1-\varepsilon)^2}{\varepsilon^3 + b}\right)u \qquad [7]$$

$$S_y = -\left(\frac{K(1-\varepsilon)^2}{\varepsilon^3 + b}\right)v + \rho g[\beta_T(T - T_r) - \beta_C(C - C_r)] \qquad [8]$$

$$S_z = -\left(\frac{K(1-\varepsilon)^2}{\varepsilon^3 + b}\right)w \qquad [9]$$

$$S_C = 0 \qquad [10]$$

where K is permeability; b is a small number to avoid division by zero; g is acceleration due to gravity; β_T is compressibility; β_C is the fractional difference in the densities of the two metals; T_r and C_r are reference temperature ($T_{melt,Ni}$) and composition (0) for buoyancy, respectively; and ε is liquid fraction. The first terms in Eq. [7] through [9] represent the porous mediumlike resistance in the mushy region at the solid-liquid interface. In the fully liquid region, the value of ε is 1, making the porous medium resistance terms zero. On the other hand, in the fully solid region, $\varepsilon = 0$, thus forcing the porous medium resistance terms in Eqs. [7] through [9] to be very large. This large negative source term offers a high flow resistance, making the velocities in the entire solid

region effectively zero. In the mushy region, however, ε lies between 0 and 1, and the porous medium resistance varies smoothly from zero in the liquid region to a high value in the solid region, thus making the velocities vary accordingly. Since the velocity in the weld pool is large, the mushy zone is expected to be very thin:

$$S_h = -\frac{\partial}{\partial t}(\rho \Delta H) \quad [11]$$

The enthalpy, H, of a material can be expressed as

$$H = h_s + \Delta H \quad [12]$$

$$h_s = cT \quad [13]$$

where h_s is the sensible heat, ΔH is the latent heat content, and c is the specific heat. In order to simulate phase change, the latent heat contribution is specified as a function of temperature, T, and the resulting expression is

$$\Delta H = f(T) \quad [14]$$

Since latent heat is associated with the liquid fraction, ε, one can write

$$\Delta H = f(T) = \begin{cases} L & \text{for} \quad T > T_l \\ L\varepsilon & \text{for} \quad T_s \le T \le T_l \\ 0 & \text{for} \quad T < T_s \end{cases} \quad [15]$$

where T_l is the liquidus temperature at which solid formation begins, T_s is the solidus temperature at which full solidification occurs, and L is the latent heat of fusion. During the melting stage, L would be the latent heat of corresponding pure metal, and during the solidification stage, a weighted average of the latent heats of the two metals would be calculated according to the composition at any location. Substituting the expression for H from Eq. [12] and Eq. [13] in the energy Eq. [5], one arrives at the following final form of the energy equation:

$$\frac{\partial}{\partial t}(\rho cT) + \nabla \cdot (\rho cT) = \nabla \cdot (k \nabla T) - \frac{\partial}{\partial t}(\rho \Delta H) \quad [16]$$

where ΔH is the latent heat content of a control volume, and ε is the liquid fraction calculated as $\Delta H/L$, with L being the latent heat of melting for the corresponding metal.

During solidification of a spot weld, the enthalpy, H, used in Eq. [15] is defined in the liquid state at any location using mixture theory as given in the following equation:

$$H = H_{Cu}C + H_{Ni}(1 - C) \quad [17]$$

where H_{Cu} and H_{Ni} are the enthalpy values of copper and nickel, respectively, at a given temperature. The melting point of any alloy is approximated as follows:

$$T_{melt} = T_{melt,Cu}C + T_{melt,Ni}(1 - C) \quad [18]$$

Equation [18] gives a weighted average of the melting points of copper ($T_{melt,Cu}$) and nickel ($T_{melt,Ni}$) as it closely follows the liquidus in the phase diagram. Since the solidification speed during spot welding is high, the mushy zone could be neglected. This assumption is justifiable since we are interested only in the composition profile at a macroscopic level.

Since no mass is added and mass transfer across all faces is assumed to be zero, there are no source terms for the species conservation equation.

Boundary and initial conditions

At time $t = 0$, the entire domain is in the solid state at room temperature. At time $t > 0$, the following boundary conditions are applied.

At the top surface of the work piece, a heat flux with a Gaussian distribution is applied, as given by

$$q''(r) = \frac{\eta Q}{\pi r_q^2} \exp\left(-\frac{r^2}{r_q^2}\right) \quad [19]$$

where η is efficiency of absorption of laser, Q is laser power, and r_q is radius of the laser beam. No mass transfer is considered at the top surface. All the sides are subjected to convective and radiative heat losses. At the flat free surface of the liquid, shear force due to surface tension (Marangoni force) is expressed as

$$\mu \left.\frac{\partial u}{\partial y}\right|_{y=h} = \left.\frac{\partial \sigma}{\partial x}\right|_{y=h} \quad [20]$$

$$\mu \left.\frac{\partial w}{\partial y}\right|_{y=h} = \left.\frac{\partial \sigma}{\partial z}\right|_{y=h} \quad [21]$$

B. *Continuous Welding*

The reference frame used for the simulation of continuous welding is a moving frame fixed to the laser. The laser moves along the z-axis with a speed w_{scan}. If (x, y, z') is the stationary coordinate system and (x, y, z) is the system in reference to the laser, then $z' = z + w_{scan}t$. The governing equations in the moving reference frame would remain the same as in Eqs. [2] through [6], except for additional source terms corresponding to the coordinate transformation.[138]

$$S_x = -\left(\frac{K(1-\varepsilon)^2}{\varepsilon^3 + b}\right)u - \frac{\partial}{\partial z}(\rho u w_{scan}) \quad [22]$$

$$S_y = -\left(\frac{K(1-\varepsilon)^2}{\varepsilon^3 + b}\right)v + \rho g[\beta_T(T - T_r) - \beta_C(C - C_r)] - \frac{\partial}{\partial z}(\rho v w_{scan}) \quad [23]$$

$$S_z = -\left(\frac{K(1-\varepsilon)^2}{\varepsilon^3 + b}\right)w - \frac{\partial}{\partial z}(\rho w w_{scan}) \quad [24]$$

$$S_h = -\frac{\partial}{\partial t}(\rho \Delta H) - \frac{\partial}{\partial z}(\rho c T w_{scan}) - \frac{\partial}{\partial z}(\rho w_{scan} \Delta H) \quad [25]$$

$$S_C = -\frac{\partial}{\partial z}(C w_{scan}) \quad [26]$$

Initial and boundary conditions

The initial and boundary conditions remain the same as in spot welding except for the additional species mass flux conditions at the phase change interface.

Melting front:

$$v_n C_l = -D\frac{\partial C_l}{\partial y} \quad [27]$$

Solidification front:

$$(1 - k_p)v_n C_l = -D\frac{\partial C_l}{\partial y} \quad [28]$$

Here, v_n is the projection of the traverse speed onto the normal to the solid-liquid boundary, C_l is the species concentration in the liquid, and D is the diffusivity. The flux of species due to partitioning at the solidification interface is given by Eq. [28]. The partition coefficient, k_p, is taken to be an averaged value for the range of compositions of liquid near the solidification interface observed in the computation.

C. *Numerical Procedure*

The three-dimensional coupled continuity, momentum, energy, and mass fraction equations along with the boundary conditions are solved numerically using a finite volume technique. The general framework of the numerical solution rests on the SIMPLER algorithm,[27] modified appropriately to accommodate phase change processes and mixing of dissimilar metals. The set of linear equations obtained were solved using a tridiagonal matrix algorithm (TDMA). The values of thermophysical data used are listed in Table I, and the process parameters used for the case study are given in Table II. A nonuniform grid of 64 × 48 × 64 is used to discretize the computational domain, with a high concentration of grids inside the weld pool.

The time-steps for computations are varied according to the stages of the melting process. The large temperature gradients in the melt pool set up a strong Marangoni convection, leading to high fluid velocities, typically of the order of 1 m/s. During the initial phase during which the weld pool shape develops, the time-steps used are small (about 0.05 ms). The descretized conservation equations are solved at each time-step and convergence is declared when the maximum of residuals in two consecutive time-steps falls below a small number, say, 5×10^{-5}.

III. RESULTS AND DISCUSSION

A. *Spot Welding*

For the dissimilar couple used in the present study, copper has a higher thermal diffusivity compared to nickel. Hence, the nickel side will experience a quicker temperature rise than copper during initial stages of the heating process. As a result, the location of maximum temperature will be shifted toward the nickel side. Depending on the rate of heating of the two metals and their respective melting points, one can expect either of the two metals to melt first. In the present case, nickel melts first, as its lower thermal diffusivity more than compensates for its higher melting point. Figure 3 shows the evolution of the weld pool as the laser heating takes place. The velocity profile is superimposed on the temperature contours to show the flow pattern and the role that it plays in the transport of heat and further evolution of the weld pool. Since the temperature coefficient of surface tension, σ_T, is negative, the value of surface tension at the location of maximum temperature is lower than that at the edges of the weld pool. Hence, on the pool surface, the fluid near the center is pulled radially

Table II. Parameters Used in the Computation

Laser power (kW)	3.5
Effective Absorptivity η	0.22
Radius of laser beam distribution (mm)	0.5
Box dimensions (mm × mm × mm)	12 × 10 × 12
Number of grids	64 × 48 × 64
w_{scan} (laser scan speed, ms^{-1})	0.008
ρ_{Cu} (density of copper, kgm^{-3})	8900
ρ_{Ni} (density of nickel, kgm^{-3})	7900
ΔH_{Cu} (latent heat of copper, Jkg^{-1})	1.88×10^5
ΔH_{Ni} (latent heat of nickel, Jkg^{-1})	2.9×10^5
g (acceleration due to gravity, ms^{-2})	9.81
β_T (compressibility)	0.45×10^{-4}
β_C (fractional difference in densities of two metals)	0.11
T_r (reference temperature, K)	1358
C_r (reference composition)	0
K (permeability)	1.0×10^9

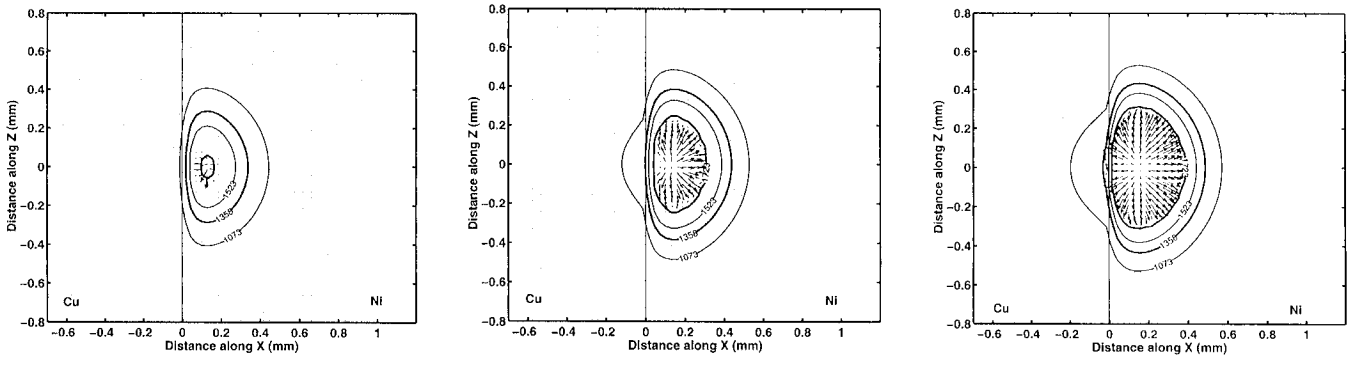

(*a*) (*b*) (*c*)

Fig. 3—Temperature contours and velocity profile of the top view of weld pool after (*a*) 1 ms, (*b*) 1.8 ms, (*c*) 2.6 ms, and (*d*) 3.4 ms, (*e*) 11 ms, and (*f*) 25 ms. Values shown on the contours are in degrees Kelvin and the bold contours refer to the melting points of copper and nickel.

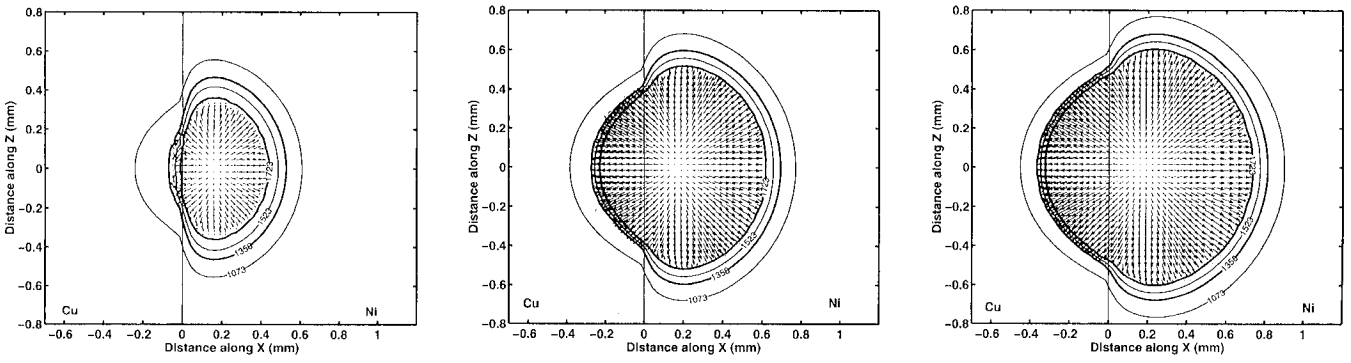

(*d*) (*e*) (*f*)

Fig. 3—(Continued). Temperature contours and velocity profile of the top view of weld pool after (*a*) 1 ms, (*b*) 1.8 ms, (*c*) 2.6 ms, and (*d*) 3.4 ms, (*e*) 11 ms, and (*f*) 25 ms. Values shown on the contours are in degrees Kelvin and the bold contours refer to the melting points of copper and nickel.

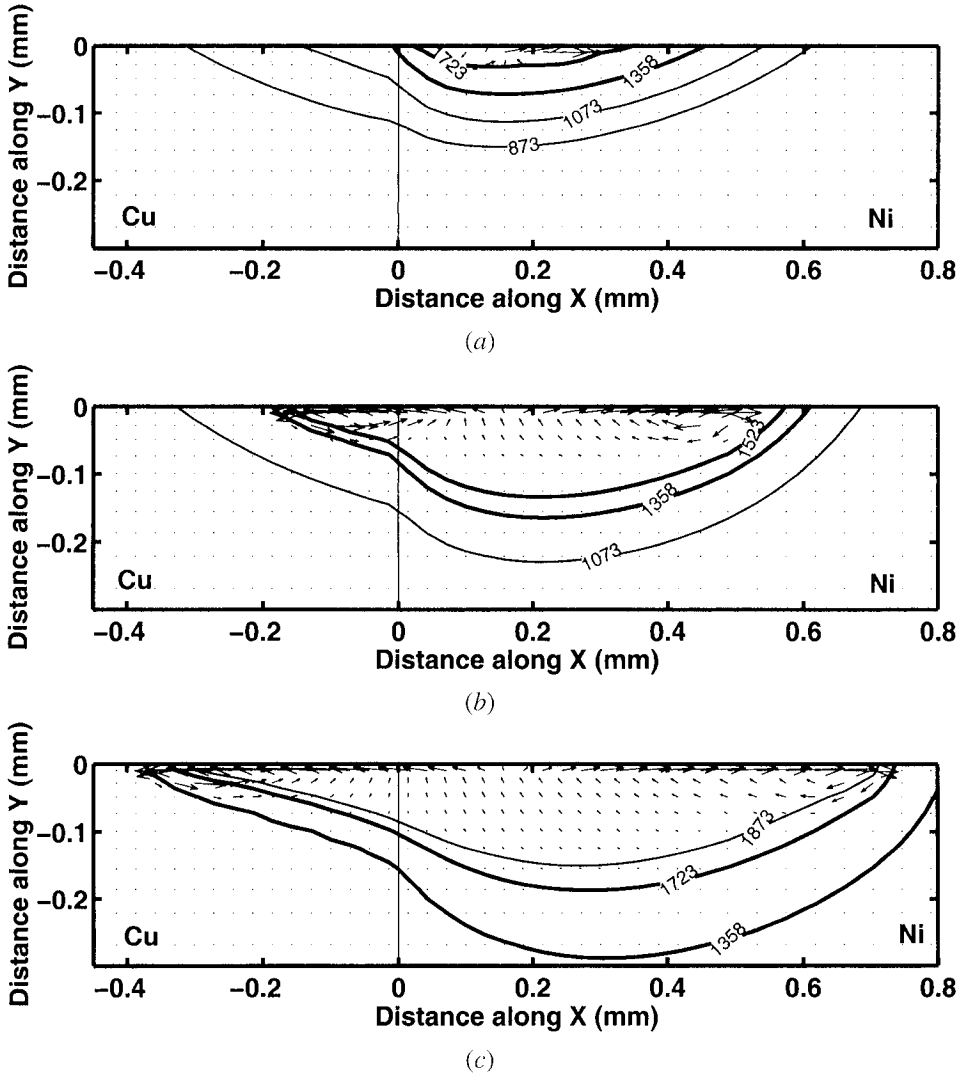

(*a*)

(*b*)

(*c*)

Fig. 4—Contours of temperature and velocity profile of the cross-sectional view of the weld pool after (*a*) 3.4 ms, (*b*) 11 ms, and (*c*) 25 ms. Values shown on the temperature contours are in degrees Kelvin.

outward. Nickel, which melts first, is convected toward the copper side by this surface-tension driven (Marangoni) flow. Hence, the initiation of melting on the copper side is aided by the flow of metal from the nickel side, in addition to direct heating by the laser. The transient formulation used in the present work allows one to follow the development

of the weld pool in this manner. This information is not easily obtainable from experiments alone.

At later times also, the flow pattern is dominated by the strong Marangoni convection originating from the nickel side. The fully developed pool shown in Figure 3(f) depicts an asymmetric shape. The evolution of the pool shape in a transverse section is shown in Figure 4. Because of asymmetric heating and convection, the isotherms bend and become noncircular. On the free surface, convection brings the hot liquid from the maximum temperature location to the edges of the weld pool, thus increasing its width. Because of continuity, the cold fluid is lifted from the bottom of the pool to the surface. The amount of heat transported in the vertical direction is therefore relatively small. As a result, the melt pool tends to be shallow and wide. As the flow is dominated by surface tension forces, the maximum velocity occurs on the free surface. The radially outward flow leads to the formation of two loops, the larger one being on the nickel side and the smaller one on the copper side. The composition distribution of copper near the top surface at three different time-steps during heating shows increased mixing as heating progresses (Figure 5). It may be noticed that the nickel side is well mixed and the composition gradients at the molten copper/substrate interface are large.

Next, we switch off the laser heat in our numerical simulation in order to study the solidification phenomena during the cooling stage. Because of the small size of the weld pool and a large base metal acting as a heat sink, cooling takes place rapidly and the weld pool shrinks, eventually leading to a completely solidified spot weld. It may be noted here that once the laser is switched off, we no longer have high-temperature gradients on the pool surface, and hence, the fluid flow in the weld pool is primarily driven by thermal buoyancy effects. The pool shapes at different time intervals during the cooling process are shown in

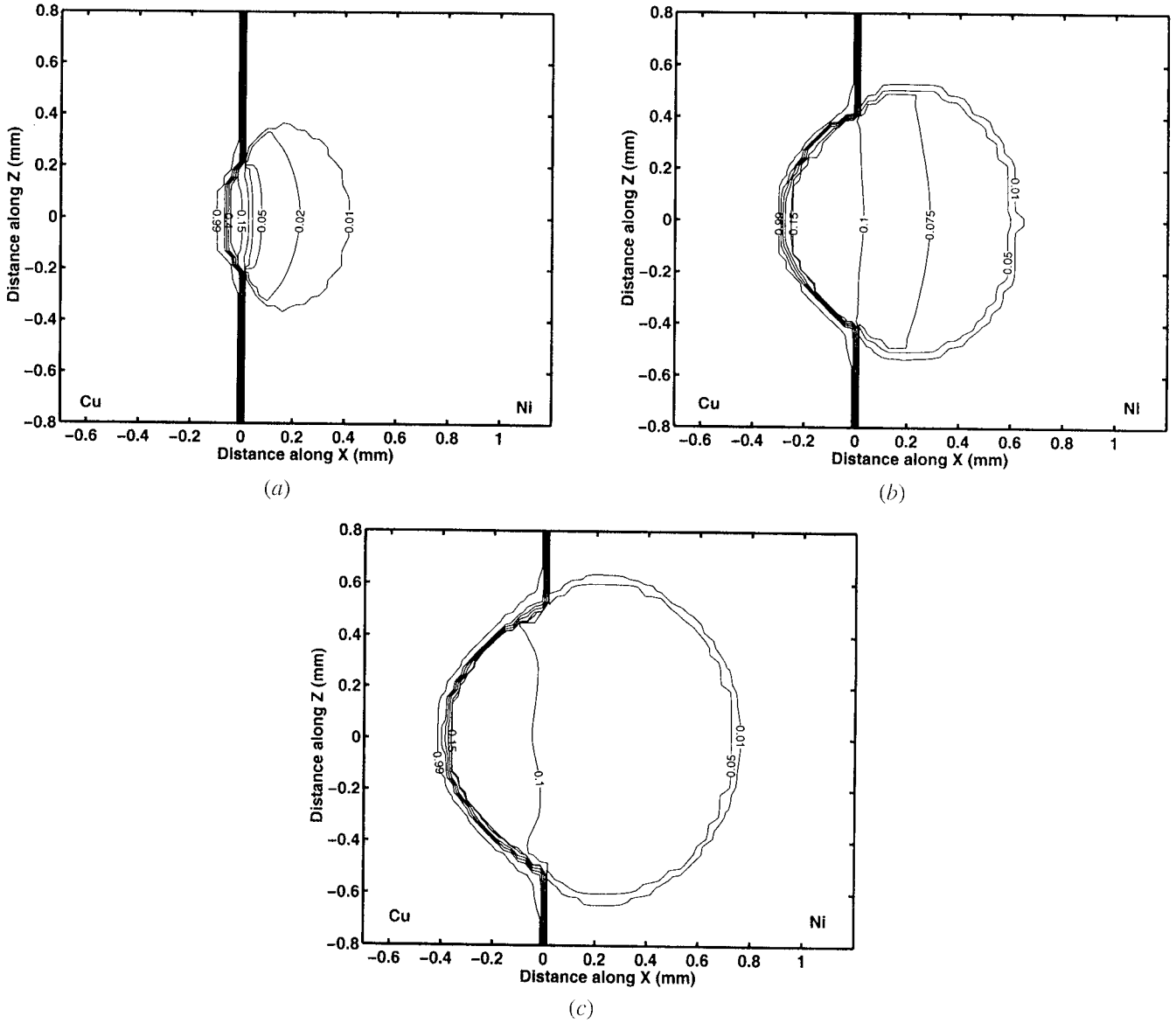

Fig. 5—Composition contours and velocity profile of the top view of weld pool after (*a*) 3.4 ms, (*b*) 11 ms, and (*c*) 25 ms. Contour labels are in Cu weight fraction.

Figure 6. Copper begins to solidify first, as its thermal diffusivity is higher than that of nickel. The cooling cycle is analyzed using the transverse section also, as shown in Figure 7. The composition of the solidified spot weld is shown in Figure 8. It may be noted that the composition is nearly uniform on the nickel side and has sharp gradients on the copper side. Not much mixing takes place during the solidification stage as the process is rapid and convection is much weaker. Hence, the solidification stage does not alter the composition profile significantly on a macroscopic scale. The solidified weld composition contours are compared with those of the experimentally determined ones, as shown in Figure 9. The asymmetry of the weld pool is clearly noticeable. The experimental and numerical plots are superimposed on Figure 9(b), and the agreement is found to be good. The asymmetric features presented here are qualitatively similar to those observed in other dissimilar couples such as Ti-Ni,[39] Ti-Al,[40] Fe-Al,[26] and Fe-Cu.[26,41]

B. *Computational Results for Continuous Welding*

The weld pool evolution during continuous welding is similar to that during spot welding. The difference, how-

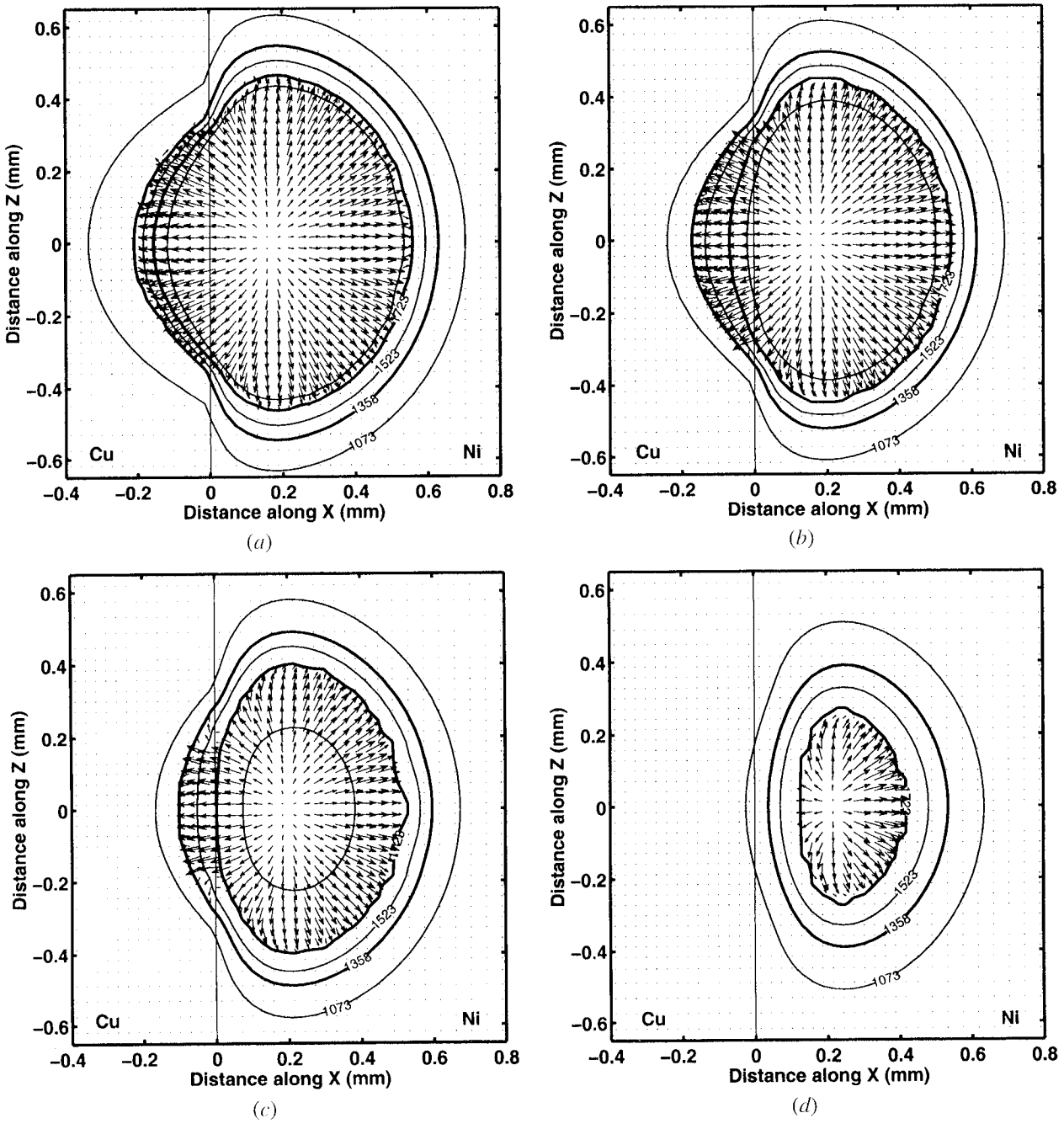

Fig. 6—Temperature contours and velocity profile in the top view during the cooling cycle: (*a*) 0 ms, (*b*) 0.3 ms, (*c*) 0.5, and (*d*) 1.1 ms after the laser is switched off.

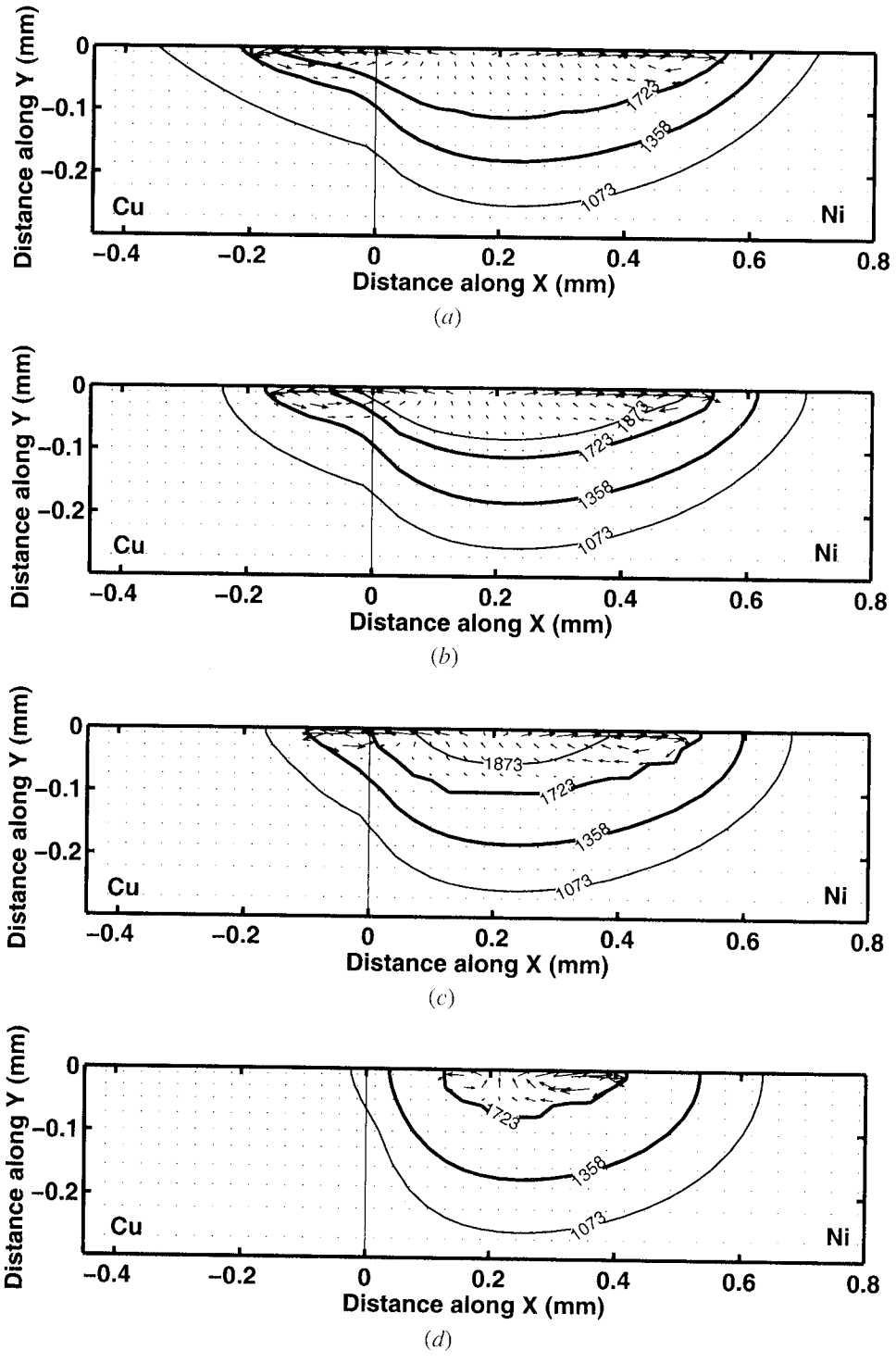

Fig. 7—Temperature contours and velocity profile in the cross-sectional view during the cooling cycle: (*a*) 0 ms, (*b*) 0.3 ms, (*c*) 0.5, and (*d*) 1.1 ms after the laser is switched off.

ever, is that the continuous weld pool becomes fully developed after the initial stage of development is over. Hence, in a reference frame moving with the laser (as used in our computational model), the pool reaches a quasi-steady state once it is fully developed. The fully developed weld pool is analyzed using temperature and velocity profiles at a particular instance. Figure 10 shows the top view and cross-sectional view of the temperature and velocity distributions. As in the case of spot welding, the weld pool is asymmetric with the nickel side being larger. It can be noted that the temperature contours are more closely spaced on the nickel side than on the copper side, indicating a higher temperature gradient on the nickel side. The velocity profile extends to the temperature contour

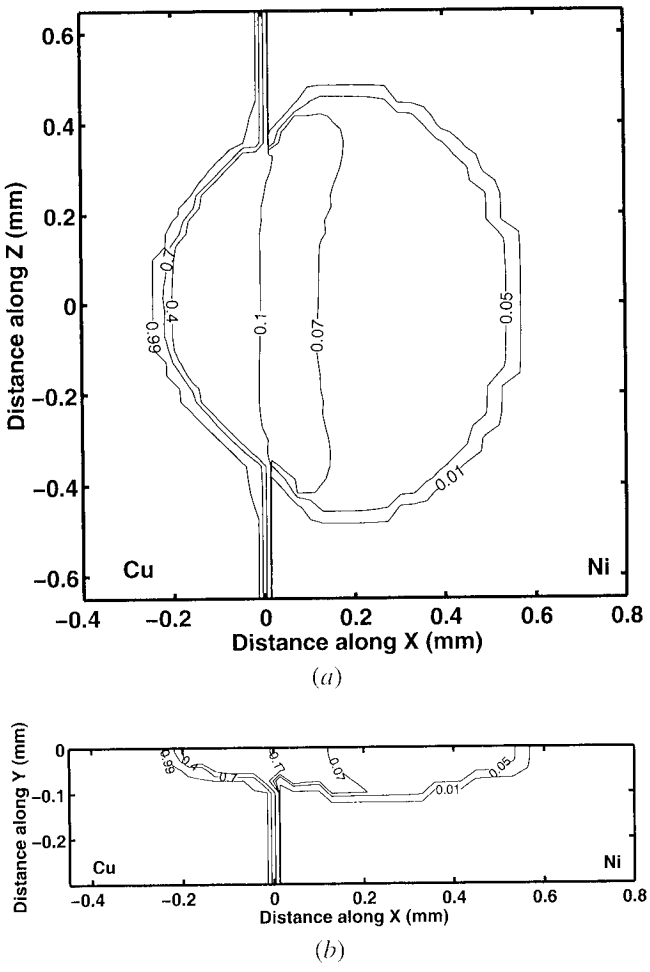

(*a*)

(*b*)

Fig. 8—Composition contours of the solidified spot weld in (*a*) top view and (*b*) cross-sectional view. Contour labels are in Cu weight fraction.

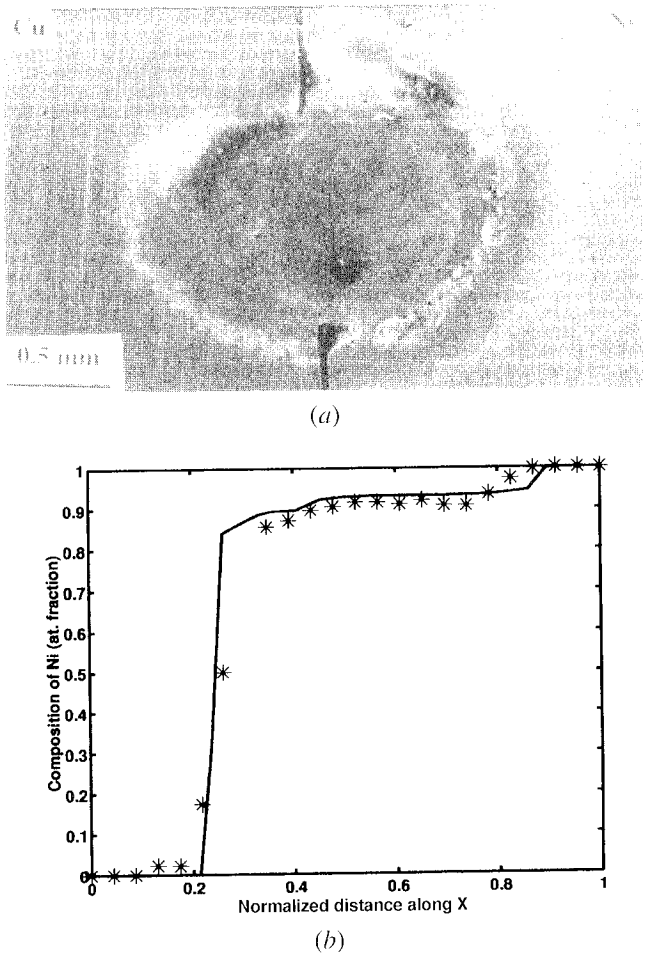

(*a*)

(*b*)

Fig. 9—(*a*) Top view of the spot weld pool processed with the same conditions as those of computation. (*b*) Composition of the solidified spot weld along a line across the weld near the top. The asterisks superimposed are the experimental compositions of nickel taken from a similar spot weld.

at 1358 K on the copper side and to the contour at 1723 K on the nickel side, showing the extent of melt pool on each side. The velocity profile shows a strong vortex on the nickel side, indicating that the weld pool shape is significantly influenced by convection on that side. The maximum velocity in the weld pool is nearly 2 m/s, which is much larger than the laser scan speed. The three-dimensional pool shape and laser scan speed can give us information regarding the time spent by a region in the molten state. The larger pool size on the nickel side indicates good mixing because of strong convection and longer duration in the molten state before solidification. On the other hand, the copper side experiences incomplete mixing, leading to sharp composition gradients. The composition contours shown in Figure 11 indicate the mixing patterns. An experimental postweld section produced from a continuous weld using the same process parameters as in the computations is shown in Figure 12(a). The asymmetry of the weld pool is clear. Also, we notice a microstructural banding (with a vortexlike appearance) on the nickel side, indicating significant convection just before solidification. A detailed composition map of the weld cross section is shown in Figure 12(b). The iso-concentration contours being parallel to the weld interface with more spacing on the nickel side indicate good mixing. Similarly, the closely spaced contours on the copper side indicate high composition gradients. These observations corroborate the findings of our computational analysis in a qualitative manner.

IV. SUMMARY

A three-dimensional computational model of the transport phenomena that take place during laser welding of dissimilar metals is developed using a finite volume formulation. The model is able to capture some of the key features of the process such as differential heating of the two metals, asymmetric weld pool development, mixing of the molten metals, and the final composition after solidification. Nickel is observed to melt first and the heat is transported to the copper side by convection in the molten nickel. The convection is primarily driven by Marangoni forces. The copper side spends less time in the liquid state and experiences insufficient mixing, whereas the nickel side is well mixed. This indicates that thermal transport controls the features of welding at a macroscopic scale.

The predicted weld pool shape and composition profile across the weld pool show good qualitative agreement with experiments.

The present work lays a foundation for future studies on some of the complex issues in dissimilar welding. Predictions about microstructure, microsegregation, and issues such

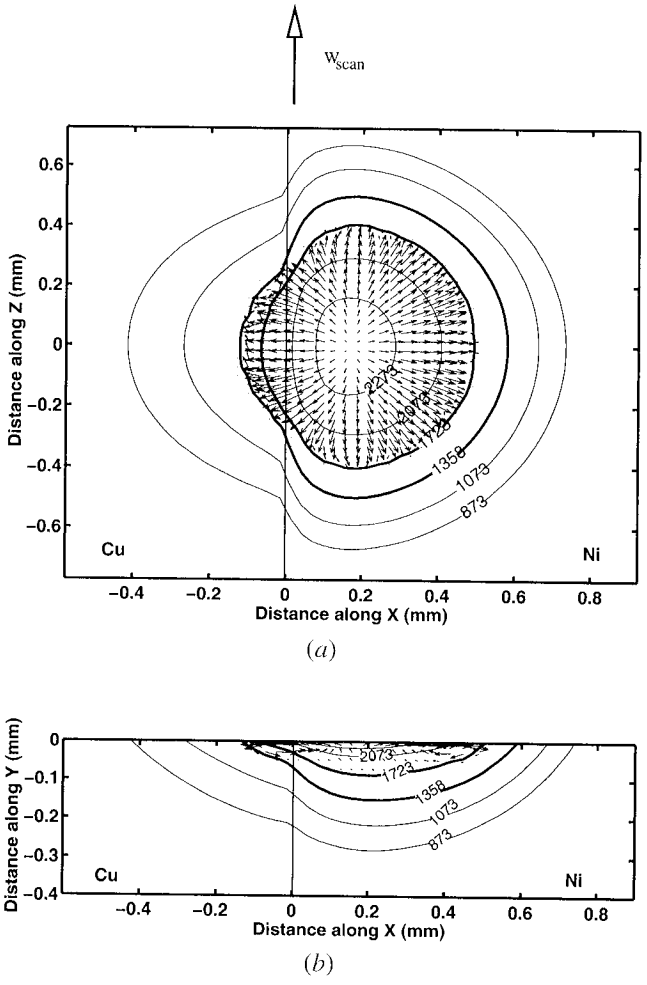

Fig. 10—Temperature contours and velocity profile in (*a*) top view and (*b*) transverse section of continuous weld at a snapshot after 7 ms.

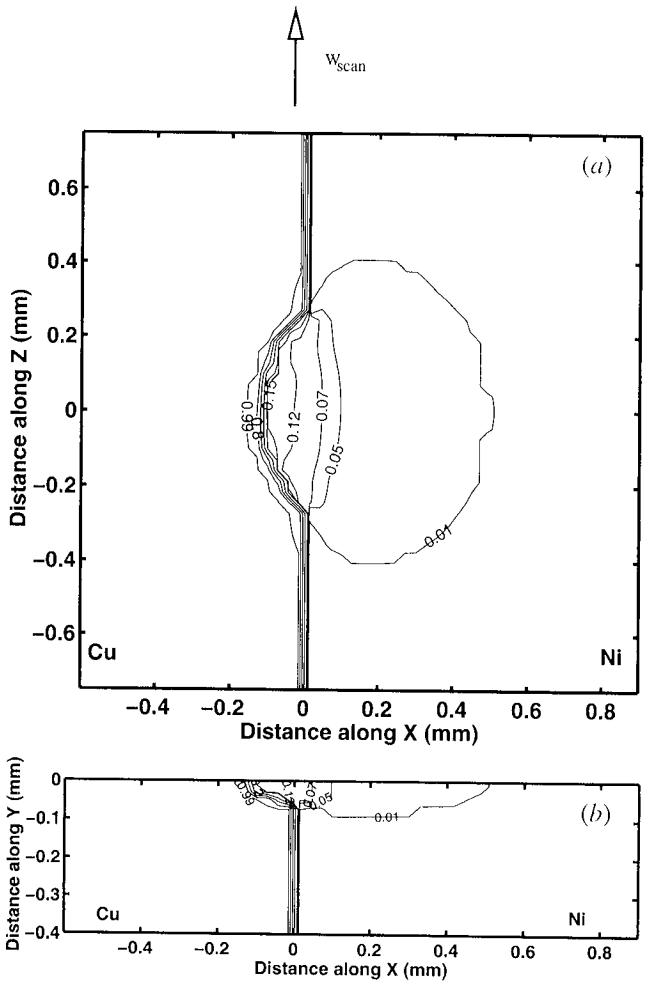

Fig. 11—Composition contours in (*a*) top view and (*b*) transverse view at a snapshot after 7 ms. Contour labels are in Cu weight fraction.

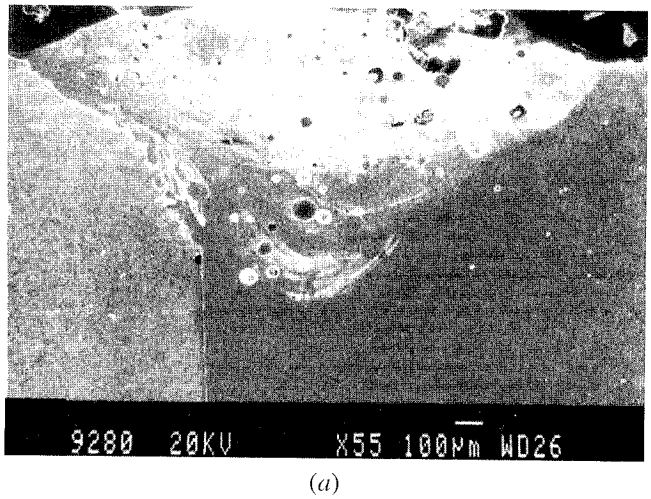

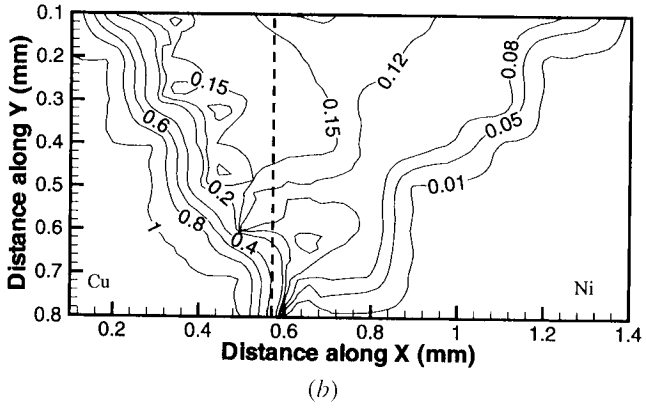

Fig. 12—(*a*) Cross-sectional view of the continuous laser weld processed with the same conditions as those of the computation. (*b*) Composition map in the whole of the weld pool with copper on the left and nickel on the right for the weld pool shown in (a). Contour labels are in Cu weight fraction.

as porosity, keyholing, and solidification cracking in dissimilar welding would require additional physical phenomena to be incorporated into the model. These aspects form some of the challenges for future studies.

ACKNOWLEDGMENTS

The authors thank the Chairman, Supercomputer Education and Research Center, Indian Institute of Science (Bangalore), for providing the computational facilities during this work.

REFERENCES

1. J. Mazumder: *J. Met.*, 1982, July, pp. 16-24.
2. J. Mazumder: *Opt. Eng.*, 1991, vol. 30, pp. 1208-19.
3. T. DebRoy and S.A. David: *Rev. Modern Phys.*, 1995, vol. 67, pp. 85-112.
4. S.A. David and J.M. Vitek: *Int. Mater. Rev.*, 1989, vol. 34, pp. 213-45.
5. C. Chan, J. Mazumder, and M.M. Chen: *Metall. Trans. A*, 1984, vol. 15A, pp. 2175-2184.
6. C.L. Chan, J. Mazumder, and M.M. Chen: *Mater. Sci. Technol.*, 1987, vol. 3, pp. 306-10.
7. T. Zacharia, A.H. Eraslan, and D.K. Aidun: *Welding J.*, 1988, vol. 67, pp. 53s-62s.
8. T. Zacharia, S.A. David, J.M. Vitek, and T. DebRoy: *Welding Res. Suppl.*, 1989, Dec., pp. 499s-509s.
9. Biswajit Basu and A.W. Date: *Int. J. Heat Mass Transfer*, 1990, vol. 33, pp. 1149-63.
10. Biswajit Basu and A.W. Date: *Int. J. Heat Mass Transfer*, 1990, vol. 33, pp. 1165-75.
11. Pradip Dutta, Yogendra Joshi, and Rama Janaswamy: *Num. Heat Transfer*, 1995, vol. 27, pp. 499-518.
12. S. Kou and Y.H. Wang: *Welding Res. Suppl.*, 1986, Mar. pp. 64s-70s.
13. A. Paul and T. DebRoy: *Metall. Trans. B*, 1988, vol. 19B, pp. 851-58.
14. Natarajan Ramanan and Seppo A. Korpela: *Metall. Trans. A*, 1990, vol. 21A, pp. 45-57.
15. A.J. Russo, R.L. Akau, and J.L. Jellison: *Welding Res. Suppl.*, 1990, Jan., pp. 23s-28s.
16. Randall L. Zehr: Ph.D. Thesis, University of Illinois at Urbana–Champaign, Urbana, IL, 1991.
17. T. Zacharia, S.A. David, J.M. Vitek, and T. DebRoy: *Welding Res. Suppl.*, 1989, Dec., pp. 510s-19s.
18. T.A. Palmer and T. DebRoy: in *Mathematical Modelling of Weld Phenomena 5*, H. Cerjak, ed., Institute of Materials, London, 2001, pp. 95-122.
19. Z. Sun and J.C. Ion: *J. Mater. Sci.*, 1995, vol. 30, pp. 4205-14.
20. S. Kumar, G. Phanikumar, P. Dutta, and K. Chattopadhyay: *J. Mater. Sci.*, 2002, vol. 37, pp. 2345-49.
21. W. Duley: *Laser Welding*, John Wiley & Sons Inc., New York, NY, 1999.
22. G. Phanikumar, R. Pardeshi, K. Chattopadhyay, P. Dutta, and J. Mazumder: *Trends in Welding Research*, Proc. 5th Int. Conf., J.M. Vitek, S.A. David, J.A. Johnson, H.B. Smartt, and T. DebRoy, eds., ASM INTERNATIONAL, Materials Park, OH, 1998, pp. 461-66.
23. G. Phanikumar, K. Chattopadhyay, and P. Dutta: *Int. J. Num. Methods Heat Fluid Flow*, 2001, vol. 11, pp. 156-71.
24. F.K. Chung and P.S. Wei: *J. Heat Transfer—Trans. ASME*, 1999, vol. 121, pp. 451-61.
25. P.S. Wei and F.K. Chung: *Metall. Mater. Trans. B*, 2000, vol. 31B, pp. 1387-1403.
26. P.S. Wei, Y.K. Kuo, and J.S. Ku: *J. Heat Transfer—Trans. ASME*, 2000, vol. 122, pp. 626-31.
27. S.V. Patankar: *Numerical Heat Transfer and Fluid Flow*, 2nd ed., Hemisphere Publications, New York, NY, 1980.
28. E.A. Brandes: *Smithells Metals Reference Book*, 6th ed., Butterworth & Co Publications Ltd., London, 1983.
29. A.D. Brent, V.R. Voller, and K.J. Reid: *Num. Heat Transfer*, 1988, vol. 13, pp. 297-318.
30. R.T.C. Choo and J. Szekely: *Welding J.*, 1994, vol. 73, pp. 25s-31s.
31. K. Hong, D.C. Weckman, and A.B. Strong: *Can. Metall. Q.*, 1998, vol. 37, pp. 293-303.
32. K. Hong, D.C. Weckman, A.B. Strong, and W. Zheng: *Sci. Technol. Welding Joining*, 2002, vol. 7 (3), pp. 125-36.
33. D.C. Weckman: in *Trends in Welding Research*, J.M. Vitek, S.A. David, J.A. Johnson, H.S. Smartt, and T. DebRoy, eds., ASM INTERNATIONAL, Materials Park, OH, 1999, p. 3.
34. Z. Yang and T. DebRoy: *Metall. Mater. Trans. B*, 1999, vol. 30B, pp. 483-93.
35. Z. Yang, J.W. Elmer, J. Wong, and T. DebRoy: *Welding J.*, 2000, vol. 79, pp. 97s-112s.
36. H. Zhao and T. DebRoy, *Metall. Mater. Trans. B*, 2001, vol. 32B, pp. 163-72.
37. J. Jaidi, K.S.S. Murthy, and P. Dutta: *Trends in Welding Research*, ASM INTERNATIONAL, Materials Park, OH, 2002, p. 147.
38. P. Mohanraj, S. Sarkar, S. Chakraborty, G. Phanikumar, P. Dutta, and K. Chattopadhyay: *Int. J. Heat Fluid Flow*, 2002, vol. 23, pp. 298-307.
39. J. Seretsky and E.R. Ryba: *Welding Res. Suppl.*, 1976, July, pp. 208s-211s.
40. B. Majumdar, R. Galun, A. Weisheit, and B.L. Mordike: *J. Mater. Sci.*, 1997, vol. 32, pp. 6191-200.
41. Gandham Phanikumar: Ph.D. Thesis, Indian Institute of Science, Bangalore, 2002.